

# Noise spectroscopy through dynamical decoupling with a superconducting flux qubit

Jonas Bylander<sup>1</sup>, Simon Gustavsson<sup>1</sup>, Fei Yan<sup>2</sup>, Fumiki Yoshihara<sup>3</sup>,  
Khalil Harrabi<sup>3†</sup>, George Fitch<sup>4</sup>, David G. Cory<sup>2,5,6</sup>,  
Yasunobu Nakamura<sup>3,7</sup>, Jaw-Shen Tsai<sup>3,7</sup> & William D. Oliver<sup>1,4</sup>

<sup>1</sup>Research Laboratory of Electronics, <sup>2</sup>Department of Nuclear Science and Engineering,  
Massachusetts Institute of Technology, Cambridge, MA 02139, USA.

<sup>3</sup>The Institute of Physical and Chemical Research (RIKEN), Wako, Saitama 351-0198, Japan.

<sup>4</sup>MIT Lincoln Laboratory, 244 Wood Street, Lexington, MA 02420, USA.

<sup>5</sup>Institute for Quantum Computing and Department of Chemistry, University of Waterloo, ON, N2L 3G1, Canada.

<sup>6</sup>Perimeter Institute for Theoretical Physics, Waterloo, ON, N2J, 2W9, Canada.

<sup>7</sup>Green Innovation Research Laboratories, NEC Corporation, Tsukuba, Ibaraki 305-8501, Japan.

<sup>†</sup>Present address: Physics Department, King Fahd University of Petroleum & Minerals, Dhahran 31261, Saudi Arabia.

April 15, 2011

## Contents

<b>A</b>	<b>Measurement set-up</b>	<b>2</b>
<b>B</b>	<b>Description of the qubit</b>	<b>3</b>
<b>C</b>	<b>Description of the read-out SQUID</b>	<b>4</b>
<b>D</b>	<b>Sensitivity to noise</b>	<b>5</b>
<b>E</b>	<b>Decoherence. Ramsey and echo phase decays — <math>1/f</math>-flux noise</b>	<b>6</b>
<b>F</b>	<b>Numerical simulations of Ramsey and echo</b>	<b>7</b>
<b>G</b>	<b>Pulse calibration</b>	<b>8</b>
<b>H</b>	<b>Dynamical-decoupling pulse sequences</b>	<b>8</b>
<b>I</b>	<b>Determination of the PSD from the CPMG-decay data</b>	<b>9</b>
I.1	Decay during pulses . . . . .	9
I.2	Relaxation . . . . .	10
I.3	Dephasing . . . . .	10



## B Description of the qubit

We fabricated our device at NEC, using the standard Dolan angle-evaporation deposition process of Al–AlO<sub>x</sub>–Al on a SiO<sub>2</sub>/Si wafer (Supplementary Fig. 1a).

The persistent-current, or flux qubit [2–5] consists of a superconducting loop with diameter  $d \sim 2 \mu\text{m}$ , interrupted by four Josephson junctions (Supplementary Fig. 1). Three of the junctions each have the Josephson energy  $E_J = 210 \text{ GHz}$ , and charging energy  $E_C = 4 \text{ GHz}$ ; the fourth is smaller by a factor  $\alpha = 0.54$ . The ratio of energy scales puts the device in the flux limit,  $E_J/E_C \approx 50$ , thus making the phases across the Josephson junctions well defined. The geometric and kinetic loop inductances are negligible compared to the Josephson inductance:

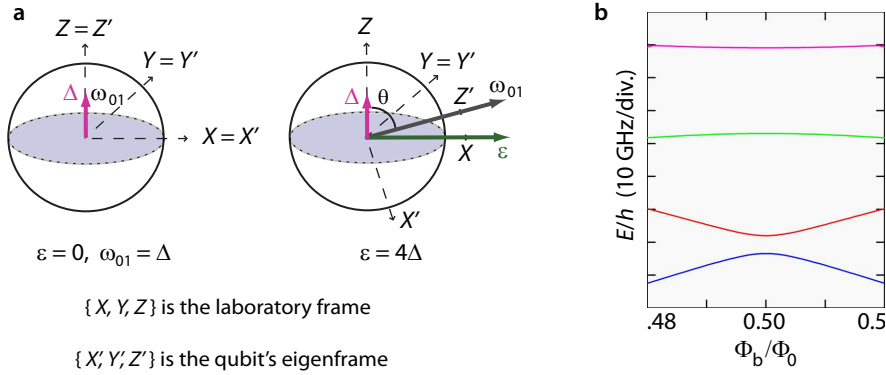
$$L_g \sim \mu_0 d \sim 2 \text{ pH}, \quad L_k = \mu_0 \lambda_L^2 l/S \sim 30 \text{ pH}, \quad L_J = \Phi_0/2\pi I_c \sim 10 \text{ nH},$$

where we used  $\lambda_L = 100 \text{ nm}$ ,  $l = 10 \mu\text{m}$ , and  $S = 20 \times 250 \text{ nm}^2$ .

When the external magnetic flux  $\Phi$  threading the qubit loop is close to half a magnetic-flux quantum,  $\Phi_0/2$ , the qubit's potential energy exhibits a double-well profile with quantized energy levels  $\pm \hbar \varepsilon/2 = \pm I_p \Phi_b$ , where  $\Phi_b = \Phi - \Phi_0/2$  is the flux bias and  $I_p = 0.18 \mu\text{A}$  the persistent current. The ground states in the left and right potential wells correspond to the diabatic states  $|L\rangle$  and  $|R\rangle$  of opposite circulating persistent currents. A tunnel coupling  $\hbar \Delta/2$  between the right- and left-well qubit states opens an energy gap,  $\hbar \Delta$ , between the ground and excited states,  $|0\rangle$  and  $|1\rangle$ , at flux degeneracy,  $\Phi_b = 0$ . The two-level Hamiltonian – analogous to a spin-1/2 particle in a magnetic field – is in the “laboratory” frame

$$\hat{\mathcal{H}} = -\frac{\hbar}{2} [(\varepsilon + \delta\varepsilon)\hat{\sigma}_x + (\Delta + \delta\Delta)\hat{\sigma}_z], \quad (1)$$

where  $\hbar \omega_{01} = \hbar \sqrt{\varepsilon^2 + \Delta^2}$  is the energy-level splitting;  $\hat{\sigma}_j$  are the Pauli matrices; and  $\delta\varepsilon$  and  $\delta\Delta$  are the noise fluctuations. The quantization axis makes an angle  $\theta = \arctan(\varepsilon/\Delta)$  with  $\hat{\sigma}_z$  (and an angle  $\pi - \theta$  with the persistent-current eigenstates), so that the qubit is first-order insensitive to flux noise when biased at the degeneracy point  $\varepsilon = 0$ . (We write the Hamiltonian in this way rather than with swapped  $x$  and  $z$  indices as in several previous papers, so that our pulses will be along  $X$  and  $Y$  in agreement with the habitual NMR language.) It can,



Supplementary Figure 2: **Two-level Hamiltonian in different eigenbases, and simulated energy spectrum.**

**a.** The Hamiltonian (1) in the “laboratory” frame  $\{X, Y, Z\}$  has the  $\varepsilon$  field (flux-bias) along  $X$ , perpendicular to the plane of the qubit loop, and the fixed tunnel coupling  $\Delta$  along  $Z$ . The Hamiltonian (2) in the qubit's eigenframe  $\{X', Y', Z'\}$  makes an angle  $\theta$  with  $Z$ . The figure shows both frames under two bias conditions ( $\varepsilon = 0$  [ $\theta = 0^\circ$ ] and  $\varepsilon = 4\Delta$ ), with the laboratory frame fixed in space. The two frames coincide when  $\varepsilon = 0$ . **b.** Simulated spectrum.

alternatively, be written in the qubit's eigenbasis,

$$\hat{\mathcal{H}} = -\frac{1}{2}\hbar(\omega_{01}\hat{\sigma}_{z'} + \delta\omega_{z'}\hat{\sigma}_{z'} + \delta\omega_{\perp'}\hat{\sigma}_{\perp'}), \quad (2)$$

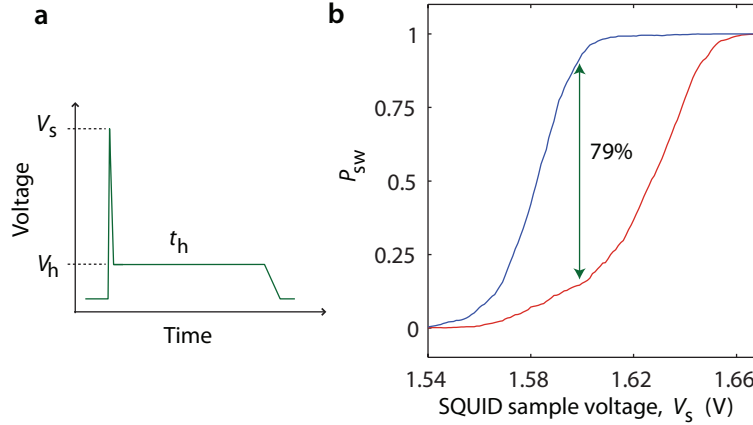
see Supplementary Fig. 2a. Here  $\hat{\sigma}_{\perp'}$  denotes that the transverse spin component can include both  $\hat{\sigma}_{x'}$  and  $\hat{\sigma}_{y'}$ . The longitudinal and transverse noises,  $\delta\omega_{z'}$  and  $\delta\omega_{\perp'}$ , are further described below.

A coil with mutual coupling  $M_{\text{dc}} = 0.6$  pH to the qubit loop provides the dc flux bias. The qubit loop is also coupled to an on-chip microwave antenna (aluminium loop launched from a coplanar waveguide towards ground) with designed mutual inductance  $M = 0.02$  pH ( $R = 50\ \Omega$  termination). This value corresponds very closely to the one inferred from a measurement of the Rabi frequency for a known applied microwave power. An amplitude of 50 mV at the generator and a total attenuation of about 56 dB corresponds to about  $-69$  dBm at the device, or an antenna current of  $I_{\mu\text{w}} \approx 1.6\ \mu\text{A}$ . The corresponding Rabi frequency is  $\Omega_{\text{R}}/2\pi = 16$  MHz, which is generated by a flux  $\Phi_{\text{R}} = \hbar\Omega_{\text{R}}/2I_{\text{P}} = 14\ \mu\Phi_0$ . The mutual inductance follows:  $M = \Phi_{\text{R}}/I_{\mu\text{w}} \approx 0.02$  pH.

As shown in Fig. 1 of the main paper, we measured remarkably long coherence times  $T_1$ ,  $T_2$  and  $T_2^*$  in this device. In nominally identical devices, we typically measure similar values for the strength of the low-frequency,  $1/f$ -type noise as in this device (section E below). In contrast, the energy-relaxation times are not as reproducible between devices; other samples from the current batch had shorter  $T_1$ .

## C Description of the read-out SQUID

Our hysteretic dc-SQUID [6], see Supplementary Fig. 1, has critical current  $I_{\text{c}} = 4.5\ \mu\text{A}$ ; normal resistance  $R_{\text{N}} = 0.25\ \text{k}\Omega$ ; mutual qubit-SQUID inductance  $M_{\text{Q-S}} = 21$  pH; on-chip capacitors  $C \sim 10$  pF, inductors  $L \sim 0.1$  nH, and bias resistors  $R_{\text{I}} = 0.2\ \text{k}\Omega$  and  $R_{\text{V}} = 1\ \text{k}\Omega$ ; and further cold and room-temperature resistors and filters. The shunt capacitors bring the plasma frequency down to  $\omega_{\text{p}}/2\pi = 2.1$  GHz.



Supplementary Figure 3: **Read-out pulse and visibility.** **a**, Read-out pulse (voltage across a 1-k $\Omega$  bias resistance). The optimized pulse shape is programmed to have a 4-ns sample pulse, including 1-ns rise, 1-ns sample, and 2-ns fall times, followed by a 3- $\mu\text{s}$  hold plateau at 17.5% of the sample voltage. **b**, Read-out visibility at  $\Phi_{\text{b}} = 0$ . Scans of the SQUID's switching probability,  $P_{\text{sw}}$ , vs. the height of the sampling pulse. We obtain 79 % read-out visibility between the qubit's ground and excited states. Relaxation during read leads to an imperfect determination of the excited state (17 % dark counts at the optimal  $V_{\text{s}}$ ).

The qubit's magnetization, resulting from the persistent currents, modulates the SQUID's switching current. For qubit read out, we apply a sample-and-hold current pulse to the SQUID (Supplementary Fig. 3a) and, after room-temperature amplification, use a threshold detector to register the presence (absence) of a voltage corresponding to the qubit being (not being) in state  $|L\rangle$ . We determine the switching probability,  $P_{\text{sw}}$ , statistically by repeating this measurement several thousand times.

The pulse is produced by a digital arbitrary-waveform generator (Tektronix AWG5014) with 250 MHz analog output bandwidth. Due to enhanced relaxation when a current is flowing through the SQUID, a rapid sample pulse is important for good read-out visibility. A hold current enables the room-temperature electronics to register the voltage pulse before retrapping occurs, but a low and short hold pulse limits the quasiparticle generation, which is also beneficial for the visibility. We obtain an optimal read-out visibility of 79% (Supplementary Fig. 3b).

In addition to biasing the SQUID, the read-out pulse couples flux into the qubit with the effect of shifting the states adiabatically,  $|0\rangle \rightarrow |L\rangle$  and  $|1\rangle \rightarrow |R\rangle$ , before the measurement takes place, so that the states can be distinguished in the persistent-current basis.

The optimal SQUID dc-bias current  $I_b$  with respect to noise coupled into the qubit was very close to  $I_b = 0$ , indicating highly symmetric SQUID junctions. In this set of experiments, we therefore did not apply any dc bias to the SQUID while manipulating the qubit, *cf.* Ref. [1].

## D Sensitivity to noise

Following the approach of Ithier *et al.* [7], we will evaluate the noise terms in the qubit's Hamiltonian,

$$\hat{\mathcal{H}} = -\frac{1}{2}\hbar(\omega_{01}\hat{\sigma}_{z'} + \delta\omega_{z'}\hat{\sigma}_{z'} + \delta\omega_{\perp'}\hat{\sigma}_{\perp'}) \quad [\text{equation (2)}].$$

We consider both flux and critical-current noise, and express the noises as sensitivity derivatives that translate the noise fluctuations to a change in the Hamiltonian, *i.e.*  $\delta\lambda \rightarrow \delta\omega$ . At  $\Phi_b = 0$ , the first-order noise  $\delta\Delta$  is much larger than second-order  $\delta\varepsilon$  (flux) noise, as confirmed through simulation. It is therefore sufficient to expand to first order to explain our Ramsey and echo data,

$$\delta\omega_{z'} = \frac{\partial\omega_{01}}{\partial\lambda}\delta\lambda + \dots \quad \text{and} \quad \delta\omega_{\perp'} = \frac{\partial\omega_{\perp'}}{\partial\lambda}\delta\lambda + \dots \quad (3)$$

Energy relaxation is related to noise that is transverse to the qubit's quantization axis,  $\delta\omega_{\perp'}(\lambda)$ , at the frequency of the level splitting  $\omega_{01}$ .

Pure dephasing, on the other hand, is related to low-frequency, longitudinal fluctuations of the qubit's energy-level splitting. To evaluate the longitudinal first-order term in equation (3) we use the chain rule,

$$\frac{\partial\omega_{01}}{\partial\lambda} = \frac{\partial\omega_{01}}{\partial\varepsilon} \frac{\partial\varepsilon}{\partial\lambda} + \frac{\partial\omega_{01}}{\partial\Delta} \frac{\partial\Delta}{\partial\lambda}. \quad (4)$$

By geometry,

$$\frac{\partial\omega_{01}}{\partial\varepsilon} = \frac{\varepsilon}{\omega_{01}} \quad \text{and} \quad \frac{\partial\omega_{01}}{\partial\Delta} = \frac{\Delta}{\omega_{01}}. \quad (5)$$

From spectroscopy measurements we infer the  $\varepsilon$  sensitivity to flux noise,  $\lambda = \Phi$ ,

$$\kappa_{\varepsilon,\Phi} \equiv \kappa_{\varepsilon} = \frac{\partial\varepsilon}{\partial\Phi} = 2\pi \times (1.1 \text{ GHz/m}\Phi_0), \quad (6)$$

while  $\Delta$  is insensitive to  $\Phi$  noise.

Since  $\hbar\varepsilon = 2I_p\Phi_b$  and  $I_p = I_c\sqrt{1 - 1/(2\alpha)^2}$ ,  $\varepsilon$  is sensitive also to critical-current noise,  $\lambda = I_c$ ,

$$\kappa_{\varepsilon,I_c} = \frac{\partial\varepsilon}{\partial I_c} = \frac{\partial\varepsilon}{\partial I_c/I_c} = \frac{\varepsilon}{I_c} I_c = \varepsilon. \quad (7)$$

For the  $\Delta$  sensitivity to fluctuations in  $i_c = \delta I_c / I_c$ , a numerical simulation gives  $\partial\Delta/\partial I_c = 2\pi \times (8 \cdot 10^{15} \text{ Hz/A})$ , and with  $I_c = 0.4 \mu\text{A}$  we obtain

$$\kappa_{\Delta, i_c} \equiv \kappa_{\Delta} = \frac{\partial\Delta}{\partial i_c} = 2\pi \times (3.2 \text{ GHz}). \quad (8)$$

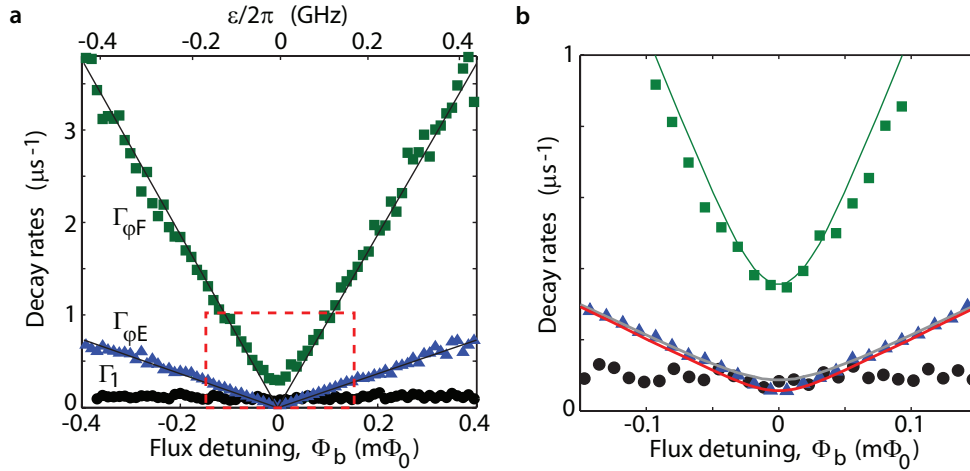
Taken together, the first-order fluctuations are therefore

$$\frac{\partial\omega_{01}}{\partial\lambda} \delta\lambda = \frac{\varepsilon}{\omega_{01}} \kappa_{\varepsilon, \Phi} \delta\Phi + \left( \frac{\varepsilon}{\omega_{01}} \kappa_{\varepsilon, i_c} + \frac{\Delta}{\omega_{01}} \kappa_{\Delta, i_c} \right) \delta i_c \quad (9)$$

Flux noise dominates, except very near  $\varepsilon = 0$ , where the  $\delta\Delta$  noise is needed to account for the observed decay (the first term is first order in  $\varepsilon$  and the second term is negligible because it is of order  $\varepsilon^2$ ).

## E Decoherence. Ramsey and echo phase decays — $1/f$ -flux noise

In the Bloch–Redfield formalism, valid for weakly coupled, short-correlated noise, the dynamics of two-level systems is described by the longitudinal and transverse relaxation rates,  $\Gamma_1 = 1/T_1$  and  $\Gamma_2 = 1/T_2$ , respectively [7, 8]. We assume that the qubit is coupled to many fluctuators, which, in concert and independent of their individual statistics, will yield a Gaussian noise distribution due to the central limit theorem. In systems where the noise is regular at the frequency of the qubit’s energy-level splitting,  $\omega_{01}$ , relaxation and dephasing factorize. The longitudinal relaxation is exponential due to the many uncorrelated contributions of transversally coupled noise at  $\omega_{01}$ . The pure-dephasing rate,  $\Gamma_{\varphi}$ , associated with low-frequency, quasi-static, longitudinally coupled noise (inhomogeneous broadening), combines with  $\Gamma_1$  to give the rate  $\Gamma_2 = \Gamma_1/2 + \Gamma_{\varphi}$ . However, the exact form of



Supplementary Figure 4: **Decay rates vs. flux detuning.** **a**, Energy-relaxation rate,  $\Gamma_1$ , and Gaussian phase-decay rates for the echo,  $\Gamma_{\varphi, E}$ , and free induction (Ramsey),  $\Gamma_{\varphi, F}$ , after subtracting the exponential  $\Gamma_1$  decay. Straight, black lines are fits to  $\Gamma_{\varphi, E/F}(\Phi_b)$  for flux noise only, see text and equation (10). **b**, Blow up of the data in the dashed-box region in **a**, along with simulated Ramsey- and echo- decay rates including both  $\delta\varepsilon$  and  $\delta\Delta$  noises. For the echo, the grey line is the rate obtained for a  $1/f$  noise in  $\delta\Delta$  with the 1-MHz high-frequency cut off given by the experimental protocol. The red line is the rate obtained with the lower high-frequency cut off:  $\omega_{\text{high}}^\lambda/2\pi < 0.1 \text{ MHz}$ . The exact rate depends on the detailed shape of the noise cut off, which is unknown.

the time dependence of the dephasing component is determined by the noise-PSD. (That is, when the dephasing is non-exponential, the inverse time constant can strictly no longer be interpreted as a simple rate.)

At  $\Phi_b = 0$ , the echo decay is nearly  $T_1$ -limited in our device and, therefore, practically indistinguishable from an exponential. Relaxation contributes by  $\Gamma_1/2 = 1/2 T_1 = 42 \times 10^3/\text{s}$  or 6.6 kHz to the low-power spectroscopic line width  $\Delta f_{(\text{FWHM})} = 180 \text{ kHz}$ . This exceeds the expected  $\Delta f_{(\text{FWHM})} = 1/\pi T_2^*$  by only 50 kHz, indicating little power broadening, given the free-induction decay rate,  $\Gamma_F = 1/T_2^*$ , with the measured  $T_2^* = 2.5 \mu\text{s}$ .

Biased away from  $\Phi_b$ , we find a Gaussian spin-echo phase decay,  $\exp[-(\Gamma_{\varphi,E} t)^2]$ , consistent with a  $1/f$  flux-noise model [7] (singular PSD at  $\omega = 0$ ). As the Ramsey fringe decays considerably faster, it is hard to distinguish between purely exponential and Gaussian decays. The bias dependencies for echo and Ramsey decays are

$$\Gamma_{\varphi,E/F}(\Phi_b) = (A_\Phi \eta_{E/F})^{1/2} \left| \frac{\partial \omega_{01}}{\partial \Phi} \right|, \quad (10)$$

where the numerical factors  $\eta$  differ due to the different echo and Ramsey filtering functions:  $\eta_{\varphi,F} = \ln(1/\omega_{\text{low}} t)$  and  $\eta_{\varphi,E} = \ln 2$ . Their ratio,  $\Gamma_{\varphi,F}(\Phi_b)/\Gamma_{\varphi,E}(\Phi_b) \approx 4.5$ , is in accordance with our data, and the magnitude,

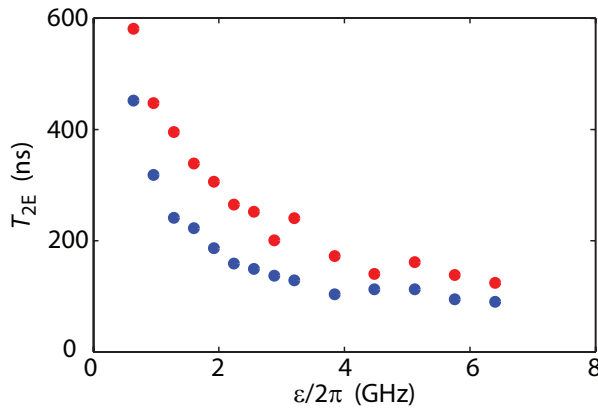
$$A_\Phi = (1.7 \mu\Phi_0)^2, \quad (11)$$

of the noise  $S(\omega) = A_\Phi/|\omega|$  agrees with previous results [1], see Supplementary Fig. 4.

The range in flux detuning covered in Supplementary Fig. 4 corresponds to a change in qubit frequency of 15 MHz. However, as shown in Supplementary Fig. 5, we can improve  $T_2$  by applying  $\pi$  pulses over a much wider range. In fact, the derivative in equation (10) reaches an asymptotic value as  $\Phi_b$  grows, and we expect the dephasing value to saturate at  $T_{2E} = 100 \text{ ns}$ . Although the Ramsey  $T_2^*$  is near zero this far detuned, the echo protocol works well, since in our qubit  $T_{2E}$  is much longer than the time  $\tau_\pi$  of one pulse.

## F Numerical simulations of Ramsey and echo

The  $\Phi_b$  dependencies of  $T_2^*$  and  $T_{2,E}$  are reproduced in numerical simulations. We simulated the Ramsey fringe by numerically solving the Bloch equations, including the measured  $T_1$  decay and linearly coupled quasi-static noises, averaging over many realizations. Each run had stochastic, normally distributed  $\delta\varepsilon$  and  $\delta\Delta$  deviations from



Supplementary Figure 5: **Echoes at large flux detuning**, Blue and red dots denote echoes with one  $\pi$  pulse and two  $\pi$  pulses, respectively (CPMG sequence, see section H below). The ratio  $T_{2E}^{(2\pi)}/T_{2E}^{(1\pi)}$  is nearly constant around 1.5 over this range.

their average values: The  $1/f$  flux noise,  $S(\omega) = A_\Phi/|\omega|$ , gives  $\sigma_\varepsilon/2\pi = 10$  MHz when integrated from 1 Hz to 1 MHz; noise in  $\Delta$  dominates near  $\Phi_b = 0$ , and we get agreement for  $\sigma_\Delta/2\pi = 0.06$  MHz, uncorrelated with the flux noise and obtained from  $S_\Delta(\omega) = A_\Delta/|\omega|$  with  $A_\Delta = (4 \cdot 10^{-6})^2$ .

In the echo simulation we additionally took into account dynamic noises from  $10^4$  to  $10^{10}$  Hz. We obtained the noisy time series for  $\varepsilon$  and  $\Delta$  by inverse-Fourier transforming the amplitudes of the  $1/f$  noises with random phases for each Fourier component, and then evaluated the Schrödinger evolution operator in discrete time.

Near  $\Phi_b = 0$ , the experimental data shows a greater echo-improvement in  $T_2$  than the simulation would suggest for these parameters (see Supplementary Fig. 4b). This discrepancy would be explained by a lower high-frequency  $\Delta$ -noise cut off, with faster decay than  $1/f$  above  $\omega_{\text{high}}^\Delta/2\pi \sim 0.1$  MHz.

Numerical evaluations of the coherence integral, equation (14) below, agree with our simulations.

## G Pulse calibration

We calibrate the rotations to  $< 1\%$  accuracy by applying a tune-up sequence of pulses, akin to methods used in NMR [9]. A rigorous measurement of gate errors should be done with randomized benchmarking, for example.

## H Dynamical-decoupling pulse sequences

Collin *et al.* [10] and Ithier *et al.* [7] have employed some NMR methods beyond the Hahn spin echo to manipulate a superconducting qubit. In this work, we apply multi-pulse, dynamical-decoupling pulse sequences to facilitate spectroscopy of the environmental noise and to significantly enhance the coherence times.

During the Carr-Purcell-Meiboom-Gill (CPMG) multi-echo sequence [11, 12], defined as

$$X_{\pi/2} - \left( \frac{\tau}{2N} - Y_\pi - \frac{\tau}{2N} \right)_N - X_{\pi/2} \quad (12)$$

and illustrated by the rotations in the Bloch sphere (Supplementary Fig. 6), the transverse component of the Bloch vector is refocused along the axis of the refocusing pulses (here  $Y$ ), whereas the perpendicular component ( $X$ ) is randomized. CPMG is a development on the Carr-Purcell (CP) sequence [11], which has identical pulse positions, but where all rotations are along the same axis. The third pulse sequence that we investigated, the Uhrig dynamical decoupling (UDD) sequence [13, 14], has normalized pulse positions defined by

$$\delta_j = \sin^2 \left( \frac{\pi j}{2N+2} \right). \quad (13)$$

The dephasing under a certain sequence is described by the *coherence integral*,

$$\chi_N(\tau) = \left( \frac{\partial \omega_{01}}{\partial \lambda} \right)^2 \tau^2 \int_0^\infty d\omega S(\omega) g_N(\omega, \tau). \quad (14)$$

Here the dimensionless filter function  $g_N(\omega, \tau)$  depends on the number and distribution of the  $\pi$  pulses [13–17],

$$g_N(\omega, \tau) = \frac{|y_N(\omega, \tau)|^2}{(\omega\tau)^2}, \quad (15)$$

$$y_N(\omega, \tau) = \left| 1 + (-1)^{1+N} \exp(i\omega\tau) + 2 \sum_{j=1}^N (-1)^j \exp(i\omega\delta_j\tau) \cos(\omega\tau_\pi/2) \right|, \quad (16)$$

where  $\delta_j \in [0, 1]$  is the normalized position of the centre of the  $j$ th  $\pi$  pulse between the two  $\pi/2$  pulses. The  $\tau_\pi$ -dependent factor assumes square pulses, but is a reasonable approximation in our case. Alternatively to equation (15), one can define a function  $F_N(\omega, \tau) = |y_N(\omega, \tau)|^2$  that filters the phase noise,  $S(\omega)/\omega^2$ , as in, *e.g.*, Refs. [13–17].



The Ramsey free induction ( $N = 0$ ) and the Hahn spin echo ( $N = 1$ ) have weighting functions  $g_0(\omega, \tau) = \text{sinc}^2(\omega\tau/2)$  and  $g_1(\omega, \tau) = \text{sinc}^2(\omega\tau/4) \sin^2(\omega\tau/4)$ , respectively. Note that  $g_1(0) = 0$ , indicating a suppression of the low-frequency part of the noise for the Hahn echo.

The CPMG sequence is inherently robust to field inhomogeneities when the following criteria are fulfilled [18]: (i) The effective rotation axis is oriented in the transverse ( $XY$ ) plane (true when the driving frequency is resonant with the level splitting); (ii) the magnetization (Bloch vector) is initially aligned with the rotation axis ( $Y$ ); and (iii) the rotation angle is  $\pi$ . Errors that occur due to deviations from (i–iii) can be quantified by computing the propagator over one cycle of the sequence. For an initial state  $Y$ , one finds that  $Y_\pi$  errors appear only to fourth order (CPMG), whereas  $X_\pi$  errors accumulate to second order (CP).

## I Determination of the PSD from the CPMG-decay data

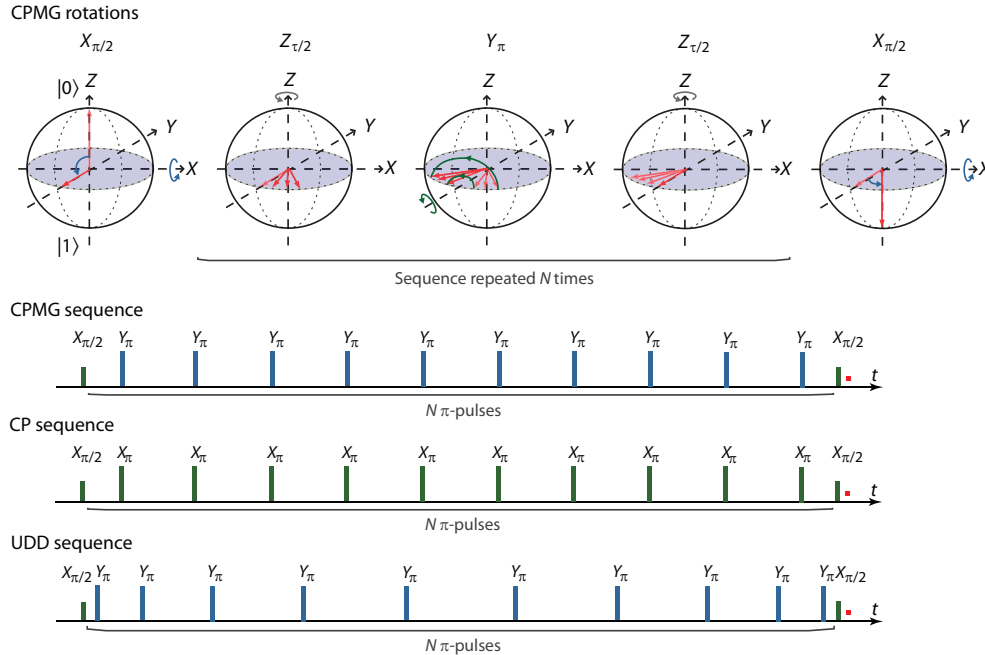
The qubit is subjected to different decay mechanisms during the CPMG pulse sequence. We identify three decay rates, and fit the qubit's population to the function

$$P_{\text{sw}}(\tau) = P_0 + a \exp(-\Gamma_1 \tau/2) \exp(-\Gamma_p(\tau_p)) \exp(-\chi_N(\tau)), \quad (17)$$

keeping the constants  $a$  and  $P_0$  fixed for all  $N$ .

### I.1 Decay during pulses

There is pulse-induced decoherence during the total pulse time  $\tau_p = N\tau_\pi + 2\tau_{3\pi/2}$ , in addition to  $T_1$  decay. (For experimental reasons, instead of  $\pi/2$  pulses we often use the functionally equivalent  $3\pi/2$  pulses.) We do not



Supplementary Figure 6: **Dynamical-decoupling pulse sequences.** Rotations of the Bloch vector during the CPMG sequence (pulses along  $X$  and  $Y$  in the laboratory frame.) Timing of the CPMG, CP, and UDD pulse sequences for  $N = 10$ .

need to assume that this decay has any particular form, *e.g.* exponential, as it will be divided out of the calculation. However, a simple exponential decay with  $\Gamma_p = 1/T_p$  where  $T_p = 1.75 \mu\text{s}$  gives a good overall fit independent of  $N$ . Although much higher than the Rabi-decay rates described in the manuscript, this rate is reasonable given that we observe an increased Rabi-decay time at high driving amplitudes (data not shown).

## I.2 Relaxation

For the duration of the sequence, there is energy relaxation with the constant rate  $\Gamma_1/2 = 1/2 T_1$ , where  $T_1 = 12 \mu\text{s}$ . We put the  $T_1$  decay during the pulses into the function  $\Gamma_p$  and therefore  $\Gamma_1/2$  in equation (17) is acting only during the free-evolution time  $\tau$ .

## I.3 Dephasing

The function  $\chi_N(\tau)$  depends on the dephasing rate during the total free-evolution time  $\tau$  under an  $N$ -pulse CPMG sequence, which provides us with a means of figuring the noise-PSD,  $S(\omega)$ . Only the PSD appears in the decay function, because the noise statistics were taken to be Gaussian, and all information is included in the second-order correlation function.

Dividing equation (17) with itself for two free-evolution times,  $\tau_1$  and  $\tau_2$ , we get

$$q(\tau_1, \tau_2) = \frac{P_{\text{sw}}(\tau_1) - P_0}{P_{\text{sw}}(\tau_2) - P_0} = \exp\left(-\Gamma_1[\tau_1 - \tau_2]\right) \exp\left(-[\chi_N(\tau_1) - \chi_N(\tau_2)]\right). \quad (18)$$

For a pulse separation  $\tau' = \tau/N$  (and large  $N$ ), the filter (15) is peaked near

$$\omega'(\tau') = \frac{2\pi}{2\tau'}. \quad (19)$$

It is narrow enough, that we can treat  $g_N(\omega'(\tau'), \tau')$  as a delta function peaked at  $\omega'$ , and regard the noise in the qubit's transition frequency as constant within its bandwidth,  $\Delta\omega$ , as illustrated in Supplementary Fig. 7a. This provides us with a means of characterizing the noise at a frequency  $\omega$  by varying  $\tau$ . We can rewrite the integral in equation (14) as  $\int_0^\infty d\omega g_N(\omega'(\tau'), \tau') \rightarrow \Delta\omega \int_0^\infty d\omega \delta(\omega - \omega')$ , and do the approximation

$$\chi_N(\tau) \approx \left(\frac{\partial\omega_{01}}{\partial\lambda}\right)^2 \tau^2 S(\omega'(\tau')) g_N(\omega'(\tau'), \tau') \Delta\omega. \quad (20)$$

We know  $\Delta\omega(\tau)$ , and  $g_N(\omega'(\tau'), \tau')$  from a numerical calculation for each  $N$ .

We can use equation (20) to evaluate the second factor on the right-hand side of equation (18),

$$\tilde{q}(\tau_1, \tau_2) = \exp\left(-\left(\frac{\partial\omega_{01}}{\partial\lambda}\right)^2 \left[\tau_1^2 S(\omega'(\tau_1)) g_{N,1}(\omega'(\tau_2), \tau_2) \Delta\omega_1 - \tau_2^2 S(\omega'(\tau_2)) g_N(\omega'(\tau_2), \tau_2) \Delta\omega_2\right]\right). \quad (21)$$

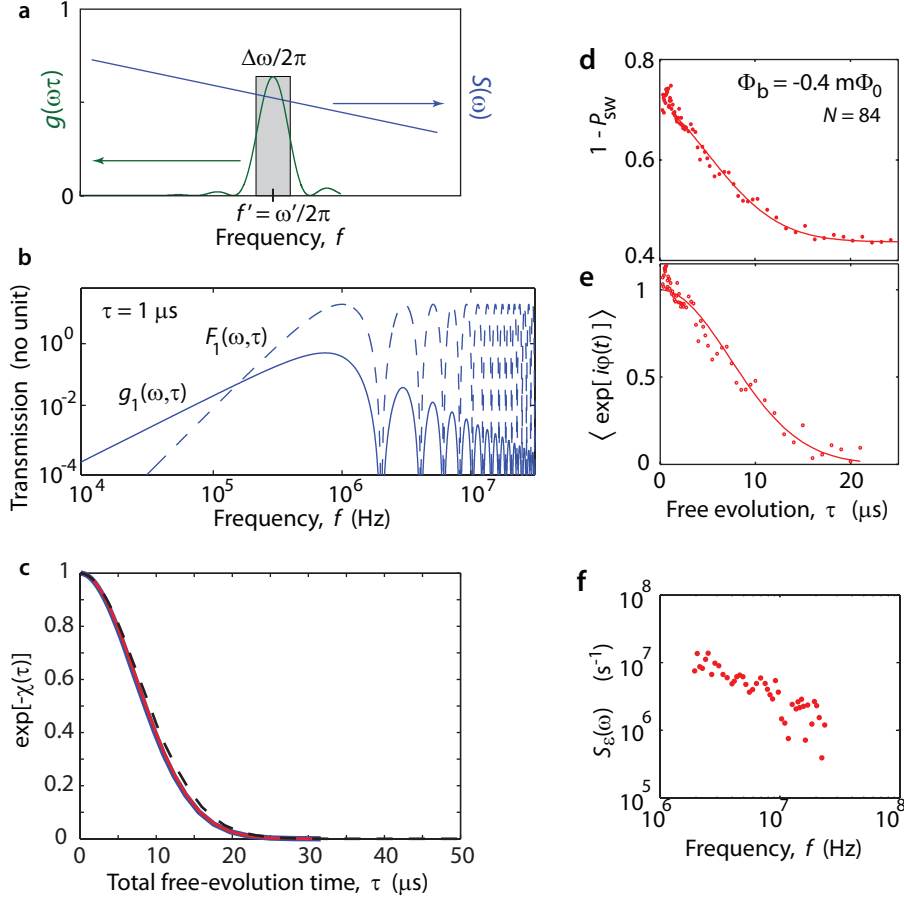
This gives us the difference between the noises at  $\omega'(\tau_1)$  and  $\omega'(\tau_2)$ , so that we can find one if we know the other. To get the absolute noise level, we have to find  $S(\omega)$  for some value of  $\omega' = \omega'(\tau')$  as a starting point. To do this, for the first point, we fix the rates  $\Gamma_p$ ,  $\Gamma_1$  and fit the dephasing using a Gaussian decay function  $\chi_N(\tau) = (\Gamma_\varphi \tau)^2$ . From that point onwards, we recursively find the remainder of the PSD using equation (20) without presuming a function form for the decay or the PSD.

Following this procedure, we obtain a number of points representing the noise PSD from 0.2 to 20 MHz. The points within the range 0.2–2 MHz lie tight together and are the least susceptible to error, which is why we fit this data to a straight line, rendering the reported  $1/f^\alpha$  dependence:  $A'_\epsilon = (0.8 \mu\Phi_0)^2$  and  $\alpha = 0.9$ . Integrating the

noise PSD from these parameters yields  $\sigma_\varepsilon = 8$  MHz (compared to 10 MHz) for the quasi-static noise, slightly changing the slope of the calculated  $\Gamma_{\varphi, F}$  in Supplementary Fig. 4, which presumed  $\alpha = 1$ . However, the slope of the PSD is not necessarily constant over many orders of magnitude, which could explain the slight deviation for the Ramsey, being sensitive to low-frequency noise.

Supplementary Figure 7c shows a numerical evaluation of the coherence integral (14), assuming a noise-PSD

$$S(\omega) = A/\omega. \quad (22)$$



Supplementary Figure 7: **Figuring the noise-PSD.** **a**, The filter function is narrow, and the noise PSD is smooth enough, that we can obtain the noise PSD at the filter's centre frequency by evaluating the coherence integral  $\chi_N(\tau)$ , equation (20). **b**, Comparison, for  $N = 1$ , of the band-pass envelope filter function  $g_N(\omega, \tau)$  used in this work to facilitate the determination of the noise-PSD (*cf.* **a**), and the high-pass envelope filter function  $F_N(\omega, \tau) = g_N(\omega, \tau) \times (\omega\tau)^2$  used in several previous works, see text. **c–f**, Fitted phase decay,  $\exp[-\chi_N(\tau)]$ , under an  $N = 84$   $\pi$ -pulse CPMG sequence with  $\tau_\pi = 6.8$  ns, at the flux detuning  $\varepsilon/2\pi = -430$  MHz ( $\Phi_0 = -0.4$  m $\Phi_0$ ), *cf.* Fig. 3b in the main text. **c**, **Blue** is the function  $\exp(-(\Gamma_\varphi^{(N)}\tau)^2)$  with a fitted  $\Gamma_\varphi^{(N)} = (8.5 \mu\text{s})^{-1}$ . **Red** is the integral (14) with  $S(\omega) = A/\omega$ . Note the excellent agreement between the blue and red lines. **Dashed** is the expression (20) with the same parameters as for the red line. **d**, Population decay under an 84-pulse CPMG sequence. Gaussian fit with fixed exponential decay contributions  $T_1 = 12 \mu\text{s}$ ,  $T_p = 1.75 \mu\text{s}$ . **e**, Phase decay of the signal in **d** after dividing out  $T_1$  and  $T_p$ . **f**, Noise-PSD calculated from the data in **e**.

The calculation shows, that this method underestimates the decay by about 5 %, since it disregards the part of the noise that falls within the harmonics of  $g_N$ , the first of which occurs at  $3\omega'$  and which is about 10 dB lower than the main lobe at  $\omega'$ .

## J Decoherence during driven evolution

We obtain information about the flux noise in the 2–20 MHz frequency range also by analyzing the decoherence during driven evolution.

Driven by a near-resonant, transverse field  $\hat{\mathcal{H}}_1 = -\hbar \Omega(t) \cos(\omega t) \hat{\sigma}_x$ , the static part of the Hamiltonian in the rotating frame is

$$\hat{\mathcal{H}} = -\frac{1}{2} \hbar (\Delta\omega \hat{\sigma}_z + \Omega \hat{\sigma}_x), \quad (23)$$

where  $\Delta\omega = \omega - \omega_{01}$ . As a result, the qubit oscillates at the Rabi frequency

$$\Omega_R = \sqrt{\Omega^2 + (\Delta\omega)^2} \approx \Omega + (\Delta\omega)^2 / 2\Omega \quad (24)$$

around the effective field, which makes an angle  $\eta = \arctan(\Delta\omega/\Omega)$  with the qubit's  $\hat{\sigma}_z$  axis.

The decay of the Rabi oscillations has contributions from noise at the frequencies  $\omega_{01}$  and  $\Omega$  [7], and from the low-frequency, quasi-static flux noise with variance  $\sigma_\varepsilon^2$ .

### J.1 Static noise

We first describe the decay due to quasi-static noise. Flux deviations from the bias point  $\varepsilon$  lead to a frequency detuning  $\Delta\omega = (\partial\omega_{01}/\partial\varepsilon)\Delta\varepsilon = (\varepsilon/\omega_{01})\Delta\varepsilon$ , normally distributed with a standard deviation  $\sigma_\varepsilon$ ,

$$N(\Delta\varepsilon) = \sigma_\varepsilon^{-1/2} \exp(-(\Delta\varepsilon)^2 / 2\sigma_\varepsilon^2). \quad (25)$$

Integrating over  $N(\Delta\varepsilon)$ , the Rabi oscillations decay as

$$\zeta(t) = \int d(\Delta\varepsilon) N(\Delta\varepsilon) \cos(\Omega_R t + \phi). \quad (26)$$

Under the approximation  $\Delta\omega \ll \Omega$ , the Fresnel-type integral (equation 26) becomes [7]

$$\zeta(t) = (1 + (ut)^2)^{-1/4} \cos\left(\Omega t + \frac{1}{2} \arctan(ut)\right), \quad (27)$$

where

$$u = \left(\frac{\partial\omega_{01}}{\partial\varepsilon}\right)^2 \frac{\sigma_\varepsilon^2}{\Omega} = \left(\frac{\varepsilon}{\omega_{01}}\right)^2 \frac{\sigma_\varepsilon^2}{\Omega}. \quad (28)$$

### J.2 Noise at the Rabi frequency

We now turn to the exponential decay of the oscillation envelope ( $\Gamma_2$  in the rotating frame),

$$\Gamma_R = \frac{3}{4}\Gamma_1 \cos^2 \theta + \frac{1}{2}\Gamma_\Omega, \quad (29)$$

where the component that depends on the noise at the Rabi frequency  $\Omega_R$  has two contributions which we denote  $\Gamma_\Omega^{(z)}$  and  $\Gamma_\Omega^{(\perp)}$ :

$$\Gamma_\Omega = \pi S_\varepsilon(\Omega_R) \sin^2 \theta + \pi S_\Delta(\Omega_R) \cos^2 \theta \equiv \Gamma_\Omega^{(z)} \sin^2 \theta + \Gamma_\Omega^{(\perp)} \cos^2 \theta. \quad (30)$$

We can approximate  $\cos^2 \theta \approx 1$ , for  $\varepsilon \ll \Delta$ , and write equation (29) as

$$\Gamma_R = \frac{3}{4}\Gamma_1 + \frac{1}{2}\Gamma_\Omega^{(\perp)} + \left(\frac{\varepsilon}{\omega_{01}}\right)^2 \frac{1}{2}\Gamma_\Omega^{(z)}. \quad (31)$$

### J.3 Fitting procedure

In order to determine  $S_\lambda(\Omega_R)$ , we measured the Rabi oscillations vs.  $\Phi_b$ , with  $\Omega_R$  fixed for each set of data. The combined decay envelope from equations (27, 31) becomes  $(1 + (ut)^2)^{-1/4} \exp(-\Gamma_R t)$ . We observe that, at  $\varepsilon = 0$ , the model predicts an exponential decay with the rate  $\frac{3}{4}\Gamma_1 + \frac{1}{2}\Gamma_\Omega^{(\perp)}$ . For a given  $\Omega_R$ , we find this rate by fitting, and then keep it fixed while fitting the Rabi envelopes vs.  $\varepsilon$ . The rate  $\Gamma_\Omega^{(\perp)}$  was too small to distinguish accurately from  $\Gamma_1$ , consistent with its correspondingly small quasi-static noise  $\sigma_{\lambda=\Delta}^2$  (Table 1 in the main text). At low amplitude ( $\Omega_R/2\pi \sim 2$  MHz),  $\Gamma_R$  nearly reaches its limit  $(3/4)\Gamma_1$ . Dividing out the known quasi-static contribution, and then fitting the envelope to the parabolic equation (31), we obtain the flux-noise dependent  $\Gamma_\Omega^{(z)}$ , from which we can calculate  $S_\varepsilon(\Omega)$ , see Fig. 4 in the main text.

## K Energy relaxation; high-frequency spectroscopy

Supplementary Figure 8 shows the variation over repeated measurements of  $T_1$  relaxation in this device.

To explain the high-frequency noise, leading to  $T_1$  relaxation, we model the  $\varepsilon$  and  $\Delta$  channels of the environment as ohmic resistors. The microwave antenna's designed mutual inductance to the qubit is  $M = 0.02$  pH with  $R = 50 \Omega$  termination. The Johnson–Nyquist (thermal and quantum) noise of an environment at  $T = 50$  mK (a reasonable effective electronic temperature on the chip) is<sup>1</sup>

$$S_\varepsilon^{\text{JN}}(\omega) = \frac{1}{2\pi} \left( \frac{\partial \varepsilon}{\partial \Phi} \right)^2 M^2 \frac{2\hbar\omega/R}{1 - e^{-\hbar\omega/k_B T}}, \quad (32)$$

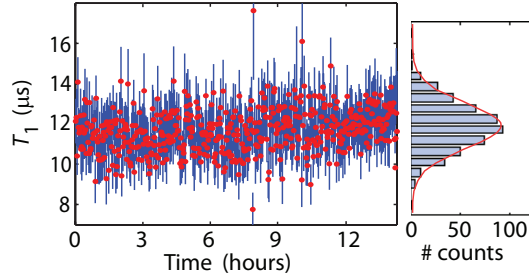
which simplifies to

$$S_\varepsilon^{\text{JN}}(\omega) \approx \frac{1}{2\pi} \left( \frac{\partial \varepsilon}{\partial \Phi} \right)^2 M^2 (2k_B T + 2\hbar\omega) / R. \quad (33)$$

This expected noise falls about 100 times below the measured PSD at  $f_{01} = \Delta/2\pi$ , indicating that intrinsic, microscopic noise mechanisms dominate the flux noise. With  $R$  unchanged, we would infer an effectively  $\sim 10$  times larger  $M$  to account for the observed noise.

Within this work, we did not identify which noise sources were responsible for the  $\delta\Delta$  noise, which can arise from, *e.g.*, critical-current noise or charge noise due to various microscopic mechanisms.

<sup>1</sup>Equation (33) is written with the following (“type 2”) definition of the Fourier transform, used throughout this paper:  $S_\lambda(\omega) = (1/2\pi) \int_{-\infty}^{\infty} dt \langle \lambda(0)\lambda(t) \rangle \exp(-i\omega t)$ , where  $\langle \cdot \rangle$  is the *un-symmetrized* correlation function.



Supplementary Figure 8:  $T_1$  **relaxation**. Repeated measurements of  $T_1$  relaxation from the excited state, at flux degeneracy  $\Phi_b = 0$ , showing how  $T_1$  varies by about 10 % from one measurement to the next. The size of the error bars from the exponential fits are on the order of the variation. Each trace took 1 min 40 s to measure;  $T_1$  may vary on a shorter time scale than that.

Taking the tilted quantization axis into account, so that the transverse noise is constituted by  $\delta\varepsilon$  noise at  $\varepsilon = 0$ , by  $\delta\Delta$  noise at  $\varepsilon \gg \Delta$ , and by combined projections of the two noises in-between, we arrive at the combined expression for the effective transverse Johnson–Nyquist noise,

$$S(\omega_{01}) = \frac{\Delta^2}{\omega_{01}^2} S_\varepsilon^{\text{JN}}(\omega_{01}) + \frac{\omega_{01}^2 - \Delta^2}{\omega_{01}^2} S_\Delta^{\text{JN}}(\omega_{01}). \quad (34)$$

As mentioned above, this *effective* noise is obviously greater than the expected extrinsic noise sources (Johnson–Nyquist as well as  $1/f$  noise). The subgap conductance, typically several hundred to several thousand times the normal resistance, may limit the achievable  $T_1$ -relaxation times [19, 20], a topic worth further studies.

## References

- [1] Yoshihara, F., Harrabi, K., Niskanen, A. O., Nakamura, Y. & Tsai, J. S. Decoherence of flux qubits due to  $1/f$  flux noise. *Phys. Rev. Lett.* **97**, 167001 (2006).
- [2] Mooij, J. E. *et al.* Josephson persistent-current qubit. *Science* **285**, 1036–1039 (1999).
- [3] Orlando, T. *et al.* Superconducting persistent-current qubit. *Phys. Rev. B* **60**, 15398–15413 (1999).
- [4] van der Wal, C. H. *et al.* Quantum superposition of macroscopic persistent-current states. *Science* **290**, 773–777 (2000).
- [5] Chiorescu, I., Nakamura, Y., Harmans, C. J. P. M. & Mooij, J. E. Coherent quantum dynamics of a superconducting flux qubit. *Science* **299**, 1869–1871 (2003).
- [6] Clarke, J. & Braginski, A. I. (eds.) *The SQUID Handbook: Fundamentals and Technology of SQUIDs and SQUID Systems Vol. I* (Wiley, Weinheim, 2004).
- [7] Ithier, G. *et al.* Decoherence in a superconducting quantum bit circuit. *Phys. Rev. B* **72**, 134519 (2005).
- [8] Geva, E., Kosloff, R. & Skinner, J. L. On the relaxation of a two-level system driven by a strong electromagnetic field. *J. Chem. Phys.* **102**, 8541–8561 (1995).
- [9] Vaughan, R. W., Elleman, D. D., Stacey, L. M., Rhim, W.-K. & Lee, J. W. A simple, low power, multiple pulse NMR spectrometer. *Rev. Sci. Instrum.* **43**, 1356–1364 (1972).
- [10] Collin, E. *et al.* NMR-like control of a quantum bit superconducting circuit. *Phys. Rev. Lett.* **93**, 157005 (2004).
- [11] Carr, H. Y. & Purcell, E. M. Effects of diffusion on free precession in nuclear magnetic resonance experiments. *Phys. Rev.* **94**, 630–638 (1954).
- [12] Meiboom, S. & Gill, D. Modified spin-echo method for measuring nuclear relaxation times. *Rev. Sci. Instrum.* **29**, 688–691 (1958).
- [13] Uhrig, G. S. Keeping a quantum bit alive by optimized  $\pi$ -pulse sequences. *Phys. Rev. Lett.* **98**, 100504 (2007).
- [14] Uhrig, G. S. Exact results on dynamical decoupling by  $\pi$  pulses in quantum information processes. *New J. Phys.* **10**, 083024 (2008).
- [15] Cywiński, L., Lutchyn, R. M., Nave, C. P. & Das Sarma, S. How to enhance dephasing time in superconducting qubits. *Phys. Rev. B* **77**, 174509 (2008).

- [16] Biercuk, M. J. *et al.* Optimized dynamical decoupling in a model quantum memory. *Nature* **458**, 996–1000 (2009).
- [17] Biercuk, M. J. *et al.* Experimental Uhrig dynamical decoupling using trapped ions. *Phys. Rev. A* **79**, 062324 (2009).
- [18] Borneman, T. W., Hurlimann, M. D. & Cory, D. G. Application of optimal control to CPMG refocusing pulse design. *J. Magn. Reson.* **207**, 220–233 (2010).
- [19] Greibe, T. *et al.* Are “pinholes” the cause of excess current in superconducting tunnel junctions? A study of Andreev current in highly resistive junctions. *Phys. Rev. Lett.* **106**, 097001 (2011).
- [20] Bezuglyi, E. V., Vasenko, A. S., Bratus, E. N., Shumeiko, V. S. & Wendin, G. Subgap current in superconducting tunnel junctions with diffusive electrodes. *Phys. Rev. B* **73**, 220506 (2006).